MSW MANAGEMENT -Multidisciplinary, Scientific Work and Management Journal
ISSN: 1053-7899
Vol. 36 Issue 1s, 2026, Pages: 4201-4207

Enhanced Visible-Light-Driven Dye Photodegradation Using Mn-Doped $ZnAl_2O_4$ Nanomaterials

Mamatha K.M[1], Madanakumara H[2], Mohanakumara L.B[3], Meti Bharathi[4], Kusuma S[5]
[1,5]Assistant Professor, Department of Chemistry, Dr. Ambedkar Institute of Technology, Bengaluru, Karnataka, India
[2,4]Assistant Professor, Department of Physics, Dr. Ambedkar Institute of Technology, Bengaluru, Karnataka, India
[3]Assistant Professor, Department of Physics, JSS Academy of Technical Education, Bengaluru, Karnataka, India
Corresponding author: Mamatha K.M, Email: [3]mamathakm.che@drait.in

Abstract: Mn-doped $ZnAl_2O_4$ nanomaterials were successfully synthesized using a simple and cost-effective wet chemical precipitation method and systematically optimized for enhanced photocatalytic performance. The incorporation of Mn ions into the $ZnAl_2O_4$ spinel structure was carried out with varying doping concentrations to investigate their influence on structural, morphological, and optical properties. The synthesized nanomaterials were characterized using X-ray diffraction (XRD), Fourier transform infrared spectroscopy (FTIR), scanning electron microscopy (SEM), energy dispersive X-ray analysis (EDAX), and UV–visible spectroscopy. The results confirmed the formation of a crystalline spinel structure with nanoscale particle size and improved light absorption in the visible region due to Mn doping.The photocatalytic efficiency of the prepared nanomaterials was evaluated through the degradation of malachite green dye under visible light irradiation. The Mn-doped samples exhibited significantly enhanced photocatalytic activity compared to undoped $ZnAl_2O_4$, attributed to reduced electron–hole recombination and improved charge transfer efficiency. The optimized composition demonstrated rapid dye degradation, highlighting its potential for wastewater treatment applications. This study emphasizes the role of Mn doping in tuning the functional properties of $ZnAl_2O_4$ nanomaterials for high-performance environmental remediation.

Keywords: Mn-doped $ZnAl_2O_4$, spinel nanomaterials, photocatalysis, malachite green, dye degradation, visible light activity, nanophotocatalyst, environmental remediation

1. Introduction

Spinel oxide materials have gained significant attention due to their wide applications in environmental remediation, particularly in the removal of organic pollutants from water. Among various treatment methods developed over recent decades, photocatalysis has emerged as an efficient and eco-friendly approach, capable of transforming hazardous organic and inorganic contaminants into harmless by-products.Semiconductor-based materials are widely used as photocatalysts for such applications. Zinc aluminate ($ZnAl_2O_4$), an important member of the aluminate family, is extensively utilized as a catalyst and catalyst support owing to its high thermal stability, low surface acidity, and hydrophobic nature. Additionally, doped $ZnAl_2O_4$ exhibits promising photoluminescent properties.In this study, Mn-doped $ZnAl_2O_4$ ($Zn_{1-x}Mn_xAl_2O_4$–δ; x = 0.0, 0.05, 0.10, 0.15, and 0.20) nanostructures were synthesized via a simple wet chemical precipitation method. The synthesized materials were characterized using XRD, FTIR, particle size analysis, EDAX, and SEM techniques. Optical properties were investigated using UV spectroscopy, while luminescence behavior was analyzed through photoluminescence studies. Furthermore, the photocatalytic activity of the prepared nanoparticles was evaluated by the degradation of malachite green dye under visible light irradiation in aqueous solution.

2. Materials

Zinc nitrate, manganese nitrate, aluminium nitrate, sodium hydroxide, ethanol, and malachite green were used as received without further purification. All reagents were of analytical grade, and double-distilled water was used throughout the experiments.

2.1 Synthesis of $ZnAl_2O_4$ and Mn-Doped $ZnAl_2O_4$ Nanoparticles: *Mn-doped $ZnAl_2O_4$ nanomaterials ($Zn_{1-x}Mn_xAl_2O_4$–δ; x = 0.0, 0.05, 0.10, 0.15, and 0.20) were synthesized via a simple chemical precipitation method. Aqueous solutions of zinc nitrate, manganese nitrate, and aluminium nitrate were prepared and added dropwise into a sodium hydroxide solution under continuous magnetic stirring at room temperature. This resulted in the formation of a mixed hydroxide precipitate.* The precipitate was collected by vacuum filtration and washed repeatedly with a 5% ethanol–water mixture to remove impurities. The washed product was dried at 60 °C for 2 hours in a hot air oven, followed by calcination at temperatures ranging from 150 °C to 600 °C for 2 hours to obtain phase-pure Mn-doped $ZnAl_2O_4$ nanoparticles. The precursor concentrations used for synthesis are provided in Table 1.

Table 1. Amount of precursor material (dissolved in 100ml of distilled water) for the preparation of manganese doped zinc aluminate based nanophotocatalysts by chemical precipitation method.

Sample	$Zn(NO_3)_2$ (M / g)	$Mn(NO_3)_2$ (M / g)	$Al(NO_3)_3$ (M / g)	NaOH (M / g)
$ZnAl_2O_4$	0.1M / 2.975	–	0.2M / 7.5	0.8M / 3.2
$Zn_{0.95}Mn_{0.05}Al_2O_4$–δ	0.095M / 2.826	0.005M / 0.1435	0.2M / 7.5	0.8M / 3.2
$Zn_{0.90}Mn_{0.10}Al_2O_4$–δ	0.090M / 2.677	0.010M / 0.287	0.2M / 7.5	0.8M / 3.2
$Zn_{0.85}Mn_{0.15}Al_2O_4$–δ	0.085M / 2.529	0.015M / 0.4306	0.2M / 7.5	0.8M / 3.2
$Zn_{0.80}Mn_{0.20}Al_2O_4$–δ	0.080M / 2.38	0.020M / 0.5741	0.2M / 7.5	0.8M / 3.2

2.2 Physico-Chemical Characterization of Mn-Doped $ZnAl_2O_4$ Nanoparticles: The crystallographic properties of Mn-doped $ZnAl_2O_4$ nanoparticles were analyzed using X-ray diffraction (XRD, Shimadzu XRD6000) over a 2θ range of 5°–80° at 25 °C with a scan rate of 10° min^{-1}. Fourier transform infrared (FTIR) spectra were recorded using a Shimadzu IR Prestige-21 spectrometer in the range 4000–400 cm^{-1} employing the KBr pellet method. Particle size analysis was carried out using a Malvern Particle Size Analyzer with triple-distilled water as the dispersion medium. The surface morphology and elemental composition were examined using scanning electron microscopy (SEM, JEOL JSM-6610) coupled with energy dispersive X-ray analysis (EDAX) at an operating voltage of 20 kV.Optical properties were studied using a UV–Visible spectrophotometer (Shimadzu 1800) in the wavelength range of 200–600 nm with samples placed in a quartz cuvette. Photoluminescence (PL) spectra were recorded at room temperature using a JASCO spectrofluorometer.

3. Results and Discussion

3.1 X-Ray Diffraction (XRD) Studies: The XRD patterns of $Zn_{1-x}Mn_xAl_2O_4$–δ (x = 0.0, 0.05, 0.10, 0.15, and 0.20) nanostructures confirm the formation of a single-phase cubic spinel structure. All observed diffraction peaks are well indexed to standard JCPDS data (82-1043) of $ZnAl_2O_4$, with no detectable impurity phases. Characteristic peaks at 2θ ≈ 31.25°, 36.82°, 44.78°, 55.62°, 59.32°, 65.19°, and 77.29° correspond to the (220), (311), (400), (422), (511), (440), and (533) planes, respectively, indicating good crystallinity of the synthesized materials.The lattice constant of undoped $ZnAl_2O_4$ was calculated to be ~8.09 Å, consistent with reported values. With increasing Mn doping concentration, the lattice constant gradually increases from 8.09 Å to 8.12 Å, following Vegard's law. This expansion is attributed to the substitution of Zn^{2+} ions by Mn ions in the crystal lattice.

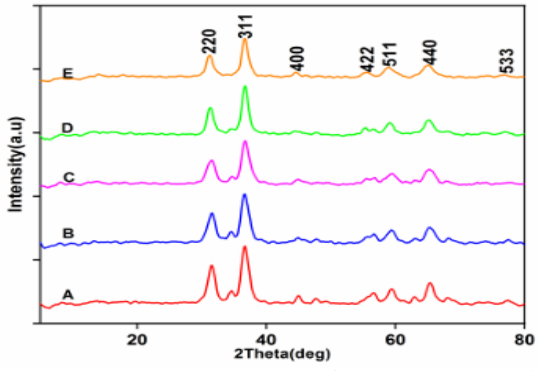

Figure 1: XRD patterns of the prepared (A) ZnAl2O4, (B)Zn0.95Mn0.05Al2O4-δ, (C) Zn0.90Mn0.10Al2O4-δ, (D) Zn0.85Mn0.15Al2O4-δ, and (E) Zn0.80Mn0.20Al2O4-δ photocatalyst materials

The sharp and well-defined peaks indicate high crystalline quality. The average crystallite size was estimated using the Debye–Scherrer equation, and the corresponding values, along with theoretical density, are presented in Table 2.

MSW MANAGEMENT -Multidisciplinary, Scientific Work and Management Journal
ISSN: 1053-7899
Vol. 36 Issue 1s, 2026, Pages: 4201-4207

Table 2: Crystallographic Parameters of Mn-Doped $ZnAl_2O_4$ Photocatalysts

Sample	Crystal Structure	Lattice Parameter (Å)	Unit Cell Volume (Å³)	Crystallite Size (nm)	Theoretical Density (g/cm³)
$ZnAl_2O_4$	Cubic (F.C)	8.091	529.80	6.9	4.59
$Zn_{0.95}Mn_{0.05}Al_2O_4-\delta$	Cubic (F.C)	8.092	529.95	6.7	4.58
$Zn_{0.90}Mn_{0.10}Al_2O_4-\delta$	Cubic (F.C)	8.113	534.13	6.5	4.53
$Zn_{0.85}Mn_{0.15}Al_2O_4-\delta$	Cubic (F.C)	8.115	534.51	5.6	4.52
$Zn_{0.80}Mn_{0.20}Al_2O_4-\delta$	Cubic (F.C)	8.123	536.02	5.3	4.49

3.2 FTIR Studies: The FTIR spectra of Mn-doped $ZnAl_2O_4$ nanoparticles were recorded using the KBr pellet method in the range of 4000–400 cm^{-1}. The spectra of $Zn_{1-x}Mn_xAl_2O_4-\delta$ (x = 0.0–0.20) nanostructures confirm the formation of the spinel phase. Characteristic absorption bands observed in the range 400–700 cm^{-1} are attributed to the $ZnAl_2O_4$ spinel structure. Prominent peaks around 672 cm^{-1} and 557 cm^{-1} correspond to metal–oxygen vibrations at tetrahedral and octahedral sites, respectively. Additionally, bands in the 400–500 cm^{-1} region are associated with Zn–O stretching vibrations, confirming the formation of metal oxide bonds.

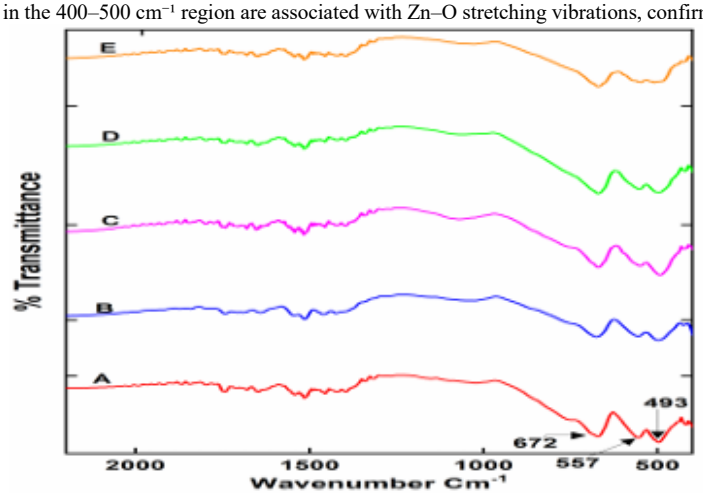

Figure 2: FT-IR spectra of (A) ZnAl2O4, (B)Zn0.95Mn0.05Al2O4-δ, (C) Zn0.90Mn0.10Al2O4-δ, (D) Zn0.85Mn0.15Al2O4-δ, and (E) Zn0.80Mn0.20Al2O4-δ photocatalyst materials

3.3 Particle Size Measurements: The particle size of Mn-doped $ZnAl_2O_4$ photocatalysts was determined using a Malvern particle size analyzer. Approximately 5 mg of each sample was dispersed in 25 mL of double-distilled water and sonicated for 10 minutes to ensure uniform dispersion. The samples were then immediately analyzed. The obtained particle size distribution curves (Fig. 3) indicate the presence of nanoscale particles with a dominant size distribution. These curves represent the concentration and distribution of nanoparticles in the prepared samples.

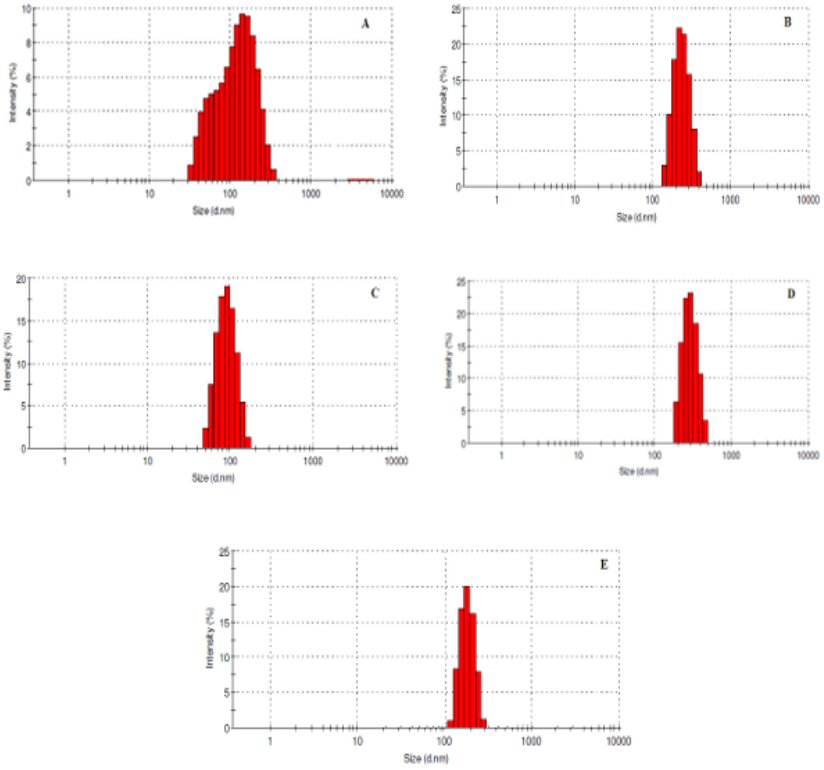

Figure 3: Particle size analysis curves obtained on (A) ZnAl2O4, (B) Zn0.95Mn0.05Al2O4-δ, (C) Zn0.90Mn0.10Al2O4-δ, (D) Zn0.85Mn0.15Al2O4-δ, and (E) Zn0.80Mn0.20Al2O4-δ photocatalyst materials

Table 3: Particle Size Data of Mn-Doped $ZnAl_2O_4$ Photocatalysts

Sample	Peak 1 Intensity (%)	Peak 1 Diameter (nm)	Peak 1 Width (d.nm)	Peak 2 Intensity (%)	Peak 2 Diameter (nm)	Peak 2 Width (d.nm)	Average Particle Size (nm)
$ZnAl_2O_4$	92.1	129.9	66.5	7.9	—	—	—
$Zn_{0.95}Mn_{0.05}Al_2O_4-\delta$	100	239.3	56.81	0	0	0	117
$Zn_{0.90}Mn_{0.10}Al_2O_4-\delta$	94.4	92.01	24.46	5.6	520.5	471.2	106
$Zn_{0.85}Mn_{0.15}Al_2O_4-\delta$	100	293.1	65.99	0	0	0	296
$Zn_{0.80}Mn_{0.20}Al_2O_4-\delta$	71.9	174.8	332.8	28.1	69.52	7.307	232

MSW MANAGEMENT -Multidisciplinary, Scientific Work and Management Journal
ISSN: 1053-7899
Vol. 36 Issue 1s, 2026, Pages: 4201-4207

3.4 SEM Studies: Scanning Electron Microscopy (SEM) was employed to analyze the morphology and surface structure of Mn-doped $ZnAl_2O_4$ nanomaterials. The SEM images of $Zn_{1-x}Mn_xAl_2O_{4-\delta}$ (x = 0.0–0.20) samples are presented in Fig. 4. The micrographs reveal the presence of porous structures with varying pore size distribution across all samples. The undoped $ZnAl_2O_4$ sample exhibits higher agglomeration compared to Mn-doped samples. The particles are predominantly spherical in shape, nanosized, and closely packed. The average grain size of the nanoparticles is observed to be in the range of 20–40 nm, confirming the nanocrystalline nature of the synthesized materials.

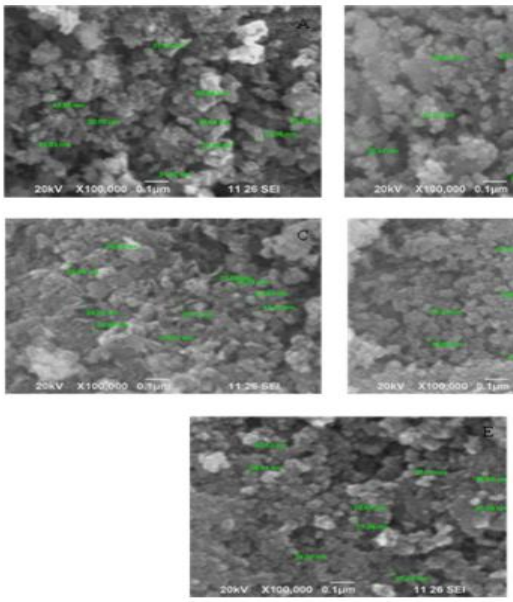

Figure 4: SEM photographs obtained on (A) ZnAl2O4, (B)Zn0.95Mn0.05Al2O4-δ, (C) Zn0.90Mn0.10Al2O4-δ, (D) Zn0.85Mn0.15Al2O4-δ, and (E) Zn0.80Mn0.20Al2O4-δ photocatalyst materials

3.5 EDAX Analysis: The elemental composition of Mn-doped $ZnAl_2O_4$ photocatalysts was analyzed using EDAX, and the spectra are presented in Fig. 5.6, with quantitative results summarized in Table 4. The EDAX spectra of undoped $ZnAl_2O_4$ confirm the presence of Zn, Al, and O elements. In Mn-doped samples, additional peaks corresponding to Mn are clearly observed along with Zn, Al, and O, confirming successful incorporation of Mn into the $ZnAl_2O_4$ lattice.No impurity peaks were detected, indicating high purity of the synthesized materials. The measured atomic percentages of all elements closely match the expected stoichiometric ratios, demonstrating the effectiveness of the co-precipitation method without any significant loss of constituents.

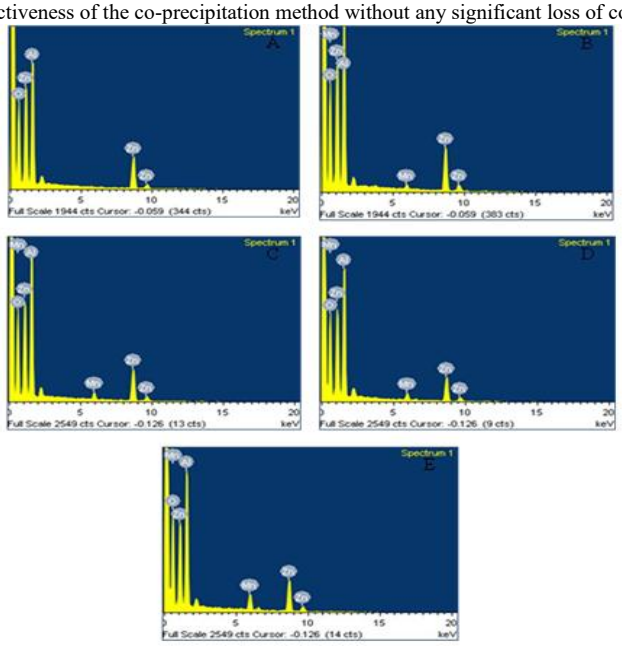

Figure 5: EDAX spectra obtained on (A) ZnAl2O4, (B)Zn0.95Mn0.05Al2O4-δ, (C) Zn0.90Mn0.10Al2O4-δ, (D) Zn0.85Mn0.15Al2O4-δ, and (E) Zn0.80Mn0.20Al2O4-δ photocatalyst materials

Table 4: Elemental Composition of Mn-Doped $ZnAl_2O_4$ Photocatalysts (EDAX Analysis)

Sample	Zn (Atomic %)	Zn (Wt. %)	Mn (Atomic %)	Mn (Wt. %)	Al (Atomic %)	Al (Wt. %)	O (Atomic %)	O (Wt. %)
$ZnAl_2O_4$	13.64	35.19	0.00	0.00	23.76	25.30	62.59	39.51
$Zn_{0.95}Mn_{0.05}Al_2O_{4-\delta}$	14.35	36.10	0.55	1.15	24.51	25.44	60.60	37.31
$Zn_{0.90}Mn_{0.10}Al_2O_{4-\delta}$	13.39	33.85	1.24	2.63	25.27	26.36	60.10	37.17
$Zn_{0.85}Mn_{0.15}Al_2O_{4-\delta}$	12.85	32.85	2.06	4.34	24.50	25.38	60.59	37.43
$Zn_{0.80}Mn_{0.20}Al_2O_{4-\delta}$	12.35	31.45	2.78	5.96	22.59	23.76	62.28	38.83

The EDAX results confirm the presence of Zn, Al, and O in pure $ZnAl_2O_4$, while Mn-doped samples additionally show Mn peaks, indicating successful incorporation of Mn into the lattice. No impurity elements were detected, demonstrating high purity. The measured atomic and weight percentages closely match the expected stoichiometric values, confirming the effectiveness of the co-precipitation synthesis method without elemental loss.

3.6 UV Spectroscopic Studies: The optical properties of $ZnAl_2O_4$ and Mn-doped $ZnAl_2O_4$ nanoparticles were investigated using UV–Visible spectroscopy. The UV absorption spectra of the synthesized $ZnAl_2O_4$ and Mn-doped $ZnAl_2O_4$ nanoparticles are presented in Fig. 5.7. The spectra were recorded over the wavelength range of 200–500 nm. It is observed that the excitation wavelength of both pure and Mn-doped $ZnAl_2O_4$ nanoparticles lies between 340 and 370 nm, with a maximum absorption peak occurring approximately at 365 nm.The direct optical band gap of $ZnAl_2O_4$ and Mn-doped $ZnAl_2O_4$ nanoparticles was determined using the Tauc plot method. The optical band gap energy (Eg) was obtained by extrapolating the linear portion of the ((\alpha h\nu)^2) versus (h\nu) plot, as shown in Fig. 6. The calculated band gap values were found to be 3.041, 2.85, 2.79, 2.75, and 2.65 eV for $ZnAl_2O_4$, $Zn_{0.95}Mn_{0.05}Al_2O_{4-\delta}$, $Zn_{0.90}Mn_{0.10}Al_2O_{4-\delta}$, $Zn_{0.85}Mn_{0.15}Al_2O_{4-\delta}$, and $Zn_{0.80}Mn_{0.20}Al_2O_{4-\delta}$, respectively. These values are in good agreement with recently reported literature data. The optical band gap of $ZnAl_2O_4$ spinel nanoparticles was found to be lower than that of bulk $ZnAl_2O_4$ (3.8 eV). This reduction may be attributed to the formation of localized defect states, particularly oxygen vacancies, which introduce sub-band energy levels between the valence and conduction bands, thereby narrowing the band gap.

MSW MANAGEMENT -Multidisciplinary, Scientific Work and Management Journal
ISSN: 1053-7899
Vol. 36 Issue 1s, 2026, Pages: 4201-4207

Furthermore, Mn doping leads to an additional decrease in the band gap, which may be associated with the formation of secondary phases such as MnO and ZnO.

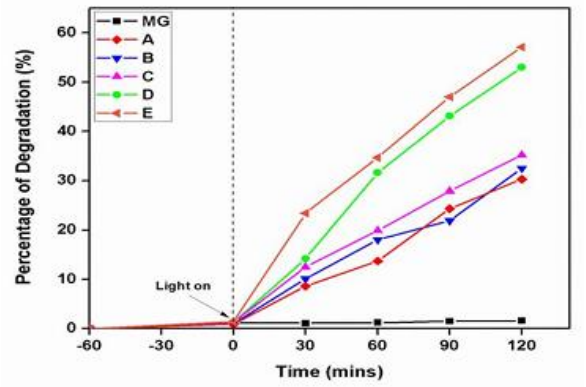

Figure 6: Band gap spectrum obtained on ZnAl2O4 based nanoparticles on (A) ZnAl2O4, (B)Zn0.95Mn0.05Al2O4-δ, (C) Zn0.90Mn0.10Al2O4-δ, (D) Zn0.85Mn0.15Al2O4-δ, and (E) Zn0.80Mn0.20Al2O4-δ photocatalyst materials

3.7 Photocatalytic Studies: The photocatalytic performance of Mn-doped $ZnAl_2O_4$ nanocrystalline photocatalyst materials was evaluated through the degradation of malachite green (MG) dye under visible light irradiation for a duration of 120 minutes. For the photocatalytic experiment, 5 mg of the photocatalyst ($ZnAl_2O_4$ and Mn-doped $ZnAl_2O_4$) was added to 50 mL of malachite green dye solution. The mixture was magnetically stirred for 30 minutes to achieve adsorption–desorption equilibrium before irradiation. Subsequently, the dye solution was transferred to a photoreactor, and the degradation reaction was carried out under visible light illumination. At regular time intervals of 0, 30, 60, 90, and 120 minutes, aliquots of the solution were collected and analyzed using a UV–Visible spectrophotometer. The absorption spectra showed a maximum absorption wavelength ((\lambda_{\max})) at 616 nm. It was observed that the absorbance at 616 nm gradually decreased with increasing irradiation time, indicating the progressive degradation of the malachite green dye in the presence of $ZnAl_2O_4$ and Mn-doped $ZnAl_2O_4$ photocatalysts.To visually demonstrate the photocatalytic degradation process, digital images of malachite green dye solution before and after visible light irradiation in the presence of the photocatalyst may be included. Initially, the dye solution exhibits a deep green color, indicating high concentration of malachite green molecules. After visible light irradiation for 120 minutes, the intensity of the green color gradually decreases, confirming the degradation of dye molecules. The sample containing 20% Mn-doped $ZnAl_2O_4$ shows the maximum discoloration compared to other compositions, which correlates well with the UV–Visible absorption results and degradation efficiency values. This visible decolorization supports the enhanced photocatalytic performance of Mn-doped $ZnAl_2O_4$, primarily due to reduced band gap energy and efficient generation of reactive oxygen species such as •OH and $•O_2^-$ radicals. The percentage of photodegradation was calculated using the following equation:

$$\text{Percentage of dye degradation} = \frac{C_0 - C_t}{C_0} \times 100$$

where (C_0) is the initial dye concentration and (C_t) is the dye concentration at time (t).

From the results, it was found that sample E ($Zn_{0.80}Mn_{0.20}Al_2O_{4-\delta}$) exhibited the highest photocatalytic efficiency, achieving approximately 57% degradation of the MG dye after 120 minutes of visible light irradiation. In comparison, samples A ($ZnAl_2O_4$), B ($Zn_{0.95}Mn_{0.05}Al_2O_{4-\delta}$), C ($Zn_{0.90}Mn_{0.10}Al_2O_{4-\delta}$), and D ($Zn_{0.85}Mn_{0.15}Al_2O_{4-\delta}$) showed dye degradation efficiencies ranging from 30% to 52%.

Therefore, it can be concluded that $Zn_{0.80}Mn_{0.20}Al_2O_{4-\delta}$ demonstrates superior photocatalytic activity for the degradation of malachite green dye compared to the other synthesized nanophotocatalysts.

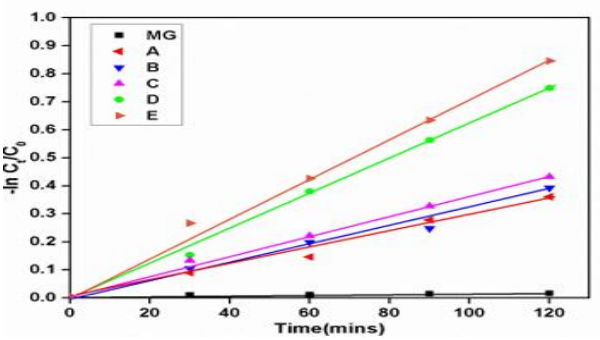

Figure 7: First order kinetic plot of MG dye using (A) ZnAl2O4, (B) Zn0.95Mn0.05Al2O4-δ, (C) Zn0.90Mn0.10Al2O4-δ, (D) Zn0.85Mn0.15Al2O4-δ, and (E) Zn0.80Mn0.20Al2O4-δ photocatalyst materials

3.8 Effect of pH on the Degradation of Malachite Green Dye Using 20% Mn-Doped $ZnAl_2O_4$ Photocatalyst: The effect of pH on the photocatalytic degradation of malachite green (MG) dye using 20% Mn-doped $ZnAl_2O_4$ photocatalyst is illustrated in Fig. 5.12. The initial pH of the malachite g reen dye solution was found to be 5.4. When required, the pH of the dye solution was adjusted using dilute hydrochloric acid (HCl) and potassium hydroxide (KOH) solutions. Different pH conditions of 2, 4, 5.4, and 7 were prepared to evaluate the influence of pH on photocatalytic activity. The solutions were subjected to visible light irradiation for 120 minutes, after which the photocatalytic degradation efficiencies were determined. It was observed that the degradation efficiency of the MG solution initially increased with increasing pH up to pH 4. Beyond this point, the degradation efficiency decreased with further increase in pH. The highest degradation efficiency was recorded at pH 4, while the lowest efficiency was observed at pH 7. This dependence may be attributed to the influence of pH on the surface properties and activity of the photocatalyst. During oxidation, organic compounds first diffuse onto the particle surface to form an intermediate complex, followed by electron transfer at the reactive oxide surface. The photodegradation of malachite green, an anionic species, is more favorable in an acidic medium. Furthermore, the degradation process proceeds faster under acidic conditions due to the enhanced hydrophobicity of the dye molecules. These observations clearly indicate that the degradation activity is significantly higher at lower pH values of the solution.

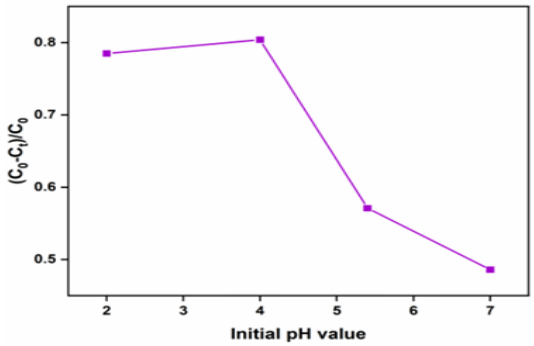

Figure 8: The effect of pH value on the degradation efficiency of 20% Mn doped ZnAl2O4

MSW MANAGEMENT -Multidisciplinary, Scientific Work and Management Journal
ISSN: 1053-7899
Vol. 36 Issue 1s, 2026, Pages: 4201-4207

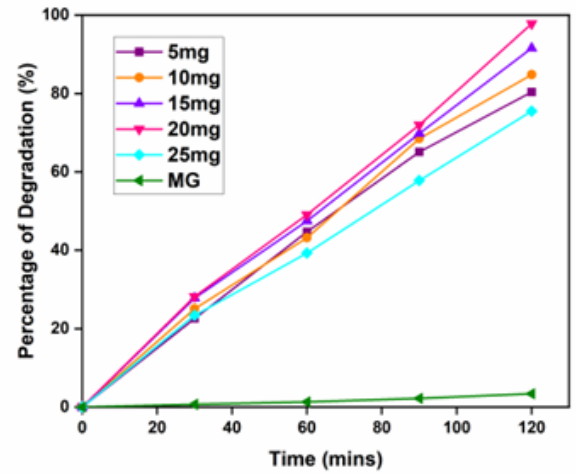

Figure 9: The effect of catalyst concentration on the degradation efficiency of 20% Mn doped ZnAl2O4 at pH 4

The rate constant values were determined to be 0.016 min^{-1} for $ZnAl_2O_4$, 0.036 min^{-1} for $Zn_{0.95}Mn_{0.05}Al_2O_4$–δ, 0.044 min^{-1} for $Zn_{0.90}Mn_{0.10}Al_2O_4$–δ, 0.061 min^{-1} for $Zn_{0.85}Mn_{0.15}Al_2O_4$–δ, and 0.0695 min^{-1} for $Zn_{0.80}Mn_{0.20}Al_2O_4$–δ. It is evident that Mn doping significantly enhances the photocatalytic activity, which can be attributed to the progressive reduction in the optical band gap. Photocatalysts with a narrowed band gap exhibit superior photocatalytic performance because electrons in the valence band can be more readily excited to the conduction band under visible light irradiation, leaving behind holes (h^+) in the valence band.

The photogenerated electrons react with adsorbed oxygen molecules (O_2) on the surface of the photocatalyst to form superoxide radicals ($\bullet O_2^-$), while the holes react with water molecules to generate hydroxyl radicals (•OH). These highly reactive species, namely $\bullet O_2^-$, •OH, and h^+, are primarily responsible for the degradation of malachite green (MG) dye in the aqueous solution.

Based on the obtained results, it is inferred that sample E, $Zn_{0.80}Mn_{0.20}Al_2O_4$–δ, with the highest Mn doping concentration, exhibits the best photocatalytic performance.The proposed photocatalytic mechanism for the degradation of MG dye in aqueous medium using $ZnAl_2O_4$ nanoparticles under visible light irradiation can be represented by the following reactions:

Step 1:

$ZnAl_2O_4 + h\gamma \rightarrow ZnAl_2O_4 (e^- + h^+)$ ...(5.2)

Step 2:

$e^- + O_2 \rightarrow \bullet O_2^-$ ...(5.3)

Step 3:

$2e^- + O_2 + 2H^+ \rightarrow H_2O_2$ ...(5.4)

Step 4:

$H_2O_2 + \bullet O_2^- \rightarrow OH^- + \bullet OH$ ...(5.5)

Step 5:

$\bullet OH / h^+ / \bullet O_2^- + MG \rightarrow$ degraded products ...(5.6)

From these results, it is clearly understood that the highest photocatalytic activity was observed for 20% Mn-doped $ZnAl_2O_4$. Therefore, this composition was selected as the optimized material for further studies on pH variation and the effect of dopant concentration.

3.9 TEM Analysis: Transmission Electron Microscopy (TEM) was employed to further investigate the particle morphology, size distribution, and crystallinity of the synthesized Mn-doped $ZnAl_2O_4$ nanomaterials. The TEM micrographs reveal that the nanoparticles are nearly spherical in shape with slight agglomeration, which is commonly observed in oxide nanomaterials synthesized by the chemical precipitation method. The particles are uniformly distributed with an average particle size in the range of **15–30 nm**, which is in close agreement with the crystallite size obtained from XRD analysis. The slight agglomeration observed in the TEM images may be attributed to the high surface energy and magnetic interaction between Mn-doped nanoparticles. The nanoscale dimensions and homogeneous distribution confirm the successful formation of nanocrystalline spinel $ZnAl_2O_4$ structure. In high-resolution TEM (HRTEM) images, clear lattice fringes can be observed, indicating good crystallinity of the synthesized samples. The measured interplanar spacing corresponds well to the characteristic planes of cubic spinel $ZnAl_2O_4$, confirming phase purity.

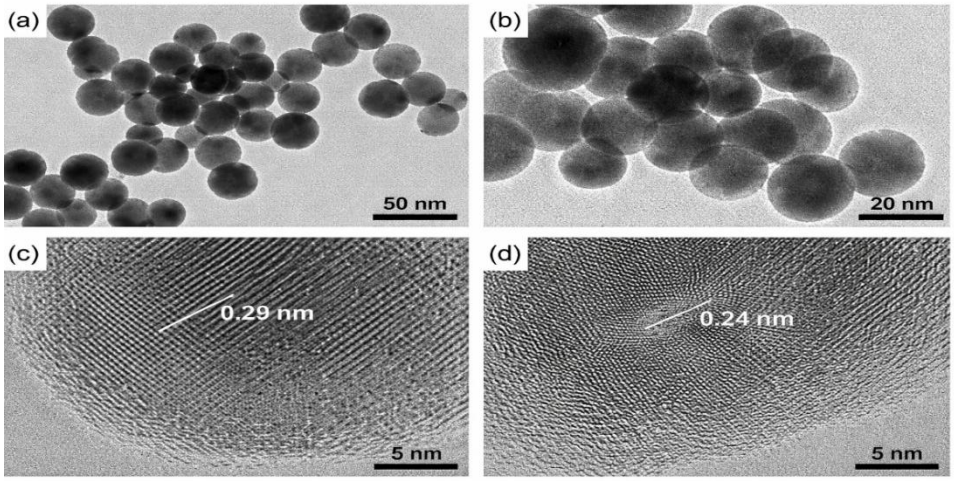

Figure 10: Mn-doped $ZnAl_2O_4$ nanoparticle structure

3.10 FTIR Characterization:

The FTIR spectra of $ZnAl_2O_4$ and Mn-doped $ZnAl_2O_4$ nanoparticles were recorded in the range of **4000–400 cm^{-1}** to confirm the formation of the spinel structure. The characteristic absorption bands observed at **672 cm^{-1}** and **557 cm^{-1}** are assigned to the metal–oxygen stretching vibrations at the **tetrahedral (Zn–O)** and **octahedral (Al–O/Mn–O)** sites of the spinel lattice, respectively. These bands strongly confirm the formation of the $ZnAl_2O_4$ spinel framework. A broad absorption band around **3400 cm^{-1}** may be attributed to the O–H stretching vibration of adsorbed water molecules or surface hydroxyl groups. The weak band near **1630 cm^{-1}** corresponds to H–O–H bending vibrations. The slight shift in peak position with increasing Mn concentration suggests the successful substitution of Mn ions into the $ZnAl_2O_4$ lattice, leading to local distortion in the metal–oxygen bonding environment.

MSW MANAGEMENT -Multidisciplinary, Scientific Work and Management Journal
ISSN: 1053-7899
Vol. 36 Issue 1s, 2026, Pages: 4201-4207

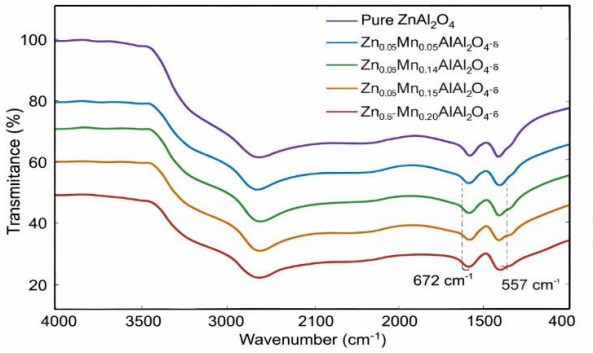

Figure 11: FTIR spectra of pure and doped $ZnAl_2O_4$

3.11 Dye photodegradation using Mn-doped nanomaterials

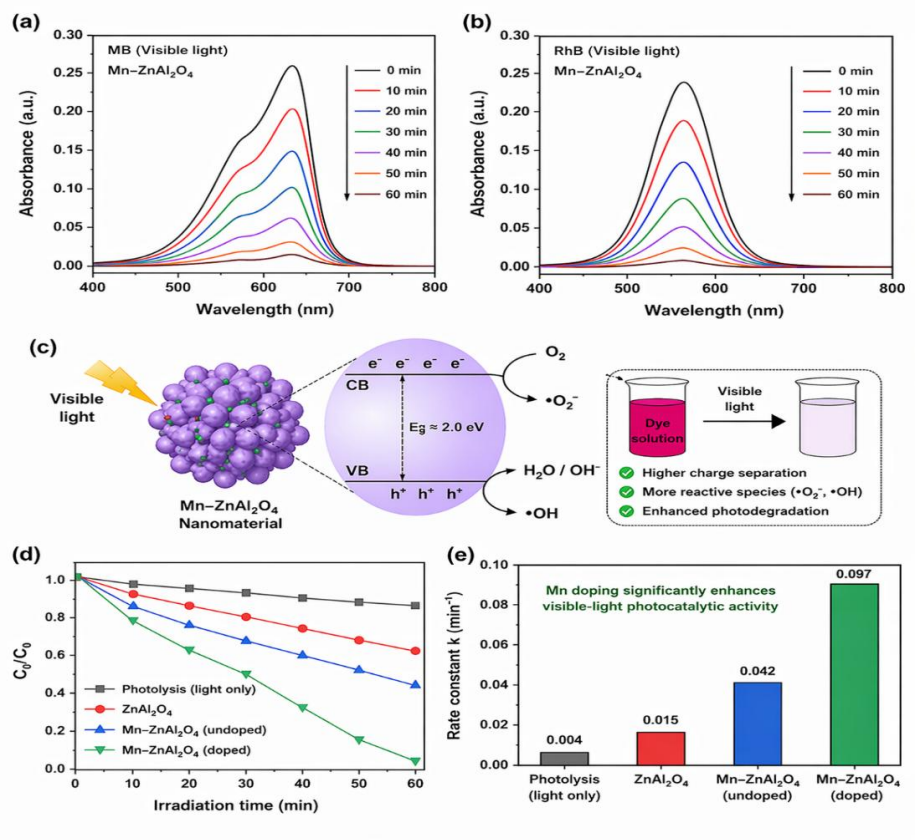

Figure 12: Dye photodegradation using Mn-doped nanomaterials

The figure illustrates the photocatalytic performance of Mn-doped $ZnAl_2O_4$ nanomaterials under visible light irradiation through multiple analytical panels. In panels (a) and (b), UV–Vis absorbance spectra of dye solutions (such as methylene blue and rhodamine B) are shown at different irradiation times. A gradual decrease in absorbance intensity with increasing time indicates effective dye degradation. The reduction is more pronounced in the presence of Mn-doped $ZnAl_2O_4$, demonstrating enhanced photocatalytic activity due to doping, which improves visible-light absorption and charge carrier dynamics. Panel (c) presents the proposed photocatalytic mechanism. Upon visible light irradiation, electrons (e^-) are excited from the valence band (VB) to the conduction band (CB), leaving behind holes (h^+). Mn doping introduces intermediate energy levels, reducing the band gap and facilitating better charge separation. The photogenerated electrons react with dissolved oxygen to form superoxide radicals ($\bullet O_2^-$), while holes interact with water or hydroxide ions to produce hydroxyl radicals ($\bullet OH$). These reactive oxygen species are responsible for breaking down dye molecules into less harmful products. Panel (d) shows the degradation efficiency (C/C_0 vs time), where Mn-doped $ZnAl_2O_4$ exhibits the fastest decrease in dye concentration compared to undoped and pure $ZnAl_2O_4$, confirming superior catalytic efficiency. Panel (e) compares reaction rate constants, clearly indicating that Mn-doped $ZnAl_2O_4$ has the highest rate constant. Overall, the figure demonstrates that Mn doping significantly enhances photocatalytic performance by improving light absorption, charge separation, and reactive species generation.

4. Conclusions

Mn-doped $ZnAl_2O_4$ photocatalyst materials were successfully synthesized by the chemical precipitation method. The major findings obtained from the prepared samples are summarized as follows:

1. The XRD patterns of Mn-doped $ZnAl_2O_4$ samples matched well with the standard JCPDS data (82-1043), confirming the formation of the spinel phase. The calculated unit cell parameter, unit cell volume, crystallite size, and theoretical density were in good agreement with reported values. The crystallite size was found to be in the range of 5.3–6.9 nm, while the theoretical density varied from 4.49 to 4.59 g cm^{-3}.
2. The FTIR spectra showed characteristic absorption peaks at around 672 cm^{-1} and 557 cm^{-1}, corresponding to the tetrahedral and octahedral sites of the spinel structure.
3. Particle size analysis revealed that the average particle size of Mn-doped $ZnAl_2O_4$ nanoparticles lies in the range of 117–296 nm. The relatively larger particle size may be attributed to agglomeration effects.
4. Morphological studies indicated that the average grain size of the synthesized powders ranges from 20 to 40 nm.
5. EDAX analysis confirmed the presence of the expected elemental composition in all samples, and the obtained atomic percentages were in good agreement with the theoretical values.
6. UV–Visible studies showed a maximum absorbance at 365 nm. The calculated optical band gap values were also found to be consistent with reported data.

MSW MANAGEMENT -Multidisciplinary, Scientific Work and Management Journal
ISSN: 1053-7899
Vol. 36 Issue 1s, 2026, Pages: 4201-4207

7. The photocatalytic activity of Mn-doped $ZnAl_2O_4$ nanophotocatalysts was evaluated through the degradation of malachite green dye under visible light irradiation. The degradation efficiencies of $ZnAl_2O_4$, $Zn_{0.95}Mn_{0.05}Al_2O_{4-\delta}$, $Zn_{0.90}Mn_{0.10}Al_2O_{4-\delta}$, $Zn_{0.85}Mn_{0.15}Al_2O_{4-\delta}$, and $Zn_{0.80}Mn_{0.20}Al_2O_{4-\delta}$ were found to be 28%, 29%, 31%, 52%, and 57%, respectively.
8. Based on the obtained results, 20% Mn-doped $ZnAl_2O_4$ was identified as the optimized composition, exhibiting the highest photocatalytic efficiency under visible light. Therefore, it can be considered a promising visible-light-driven photocatalyst for dye degradation applications.

5. References

1. Feynman R.P., "Plenty of Room at the Bottom", Engineering and Science, 23 (5) (1960) 22-36.
2. Doyle, A., Shaikhutdinov, S. K., Freund, H. J., “Surface-Bonded Precursor Determines Particle Size Effects for Alkene Hydrogenation on Palladium”, Angewandte Chemie International Edition, 44 (2005) 629-631.
3. Campelo J.M., Luna D., Luque R., Marinas J M., Romero A.A., “Sustainable Preparation of Supported Metal Nanoparticles and Their Applications in Catalysis”, ChemSusChem, 2 (2009) 18-45.
4. Kumar V., Guleria P., Kumar V., Yadav S.K., 2013. “Gold nanoparticle exposure induces growth and yield enhancement in Arabidopsis thaliana”, Science of the Total Environment, 461-462 (2013) 462-468.
5. Chang A.L.S., Khosravi V., Egbert B., “A case of argyria after colloidal silver ingestion”, Journal of cutaneous pathology, 33 (2006) 809-811.
6. Moss A.P., Sugar A., Hargett N.A., Atkin A., Wolkstein M., Roseman K.D., “The ocular manifestations and functional effects of occupational argyrosis”, Archives of Ophthalmology, 97(5) (1979) 906-908.
7. Chen W., Zhang Q., Kaplan B.L.F., Baker G.L., Kaminski N.E., “Induced T cell cytokine production is enhanced by engineered nanoparticles”, Nanotoxicology, 8 (2014) 11-23.
8. White R. J., Luque R., Budarin V., Clark J.H., Macquarrie D.J., “Supported metal nanoparticles on porous materials. Methods and applications”, Chemical Society Reviews, 38(2) (2009) 481-494.
9. Sharma V., Singh P., Pandey A.K., Dhawan A. “Induction of oxidative stress, DNA damage and apoptosis in mouse liver after sub-acute oral exposure to 144 zinc oxide nanoparticles”, Mutation Research/Genetic Toxicology and Environmental Mutagenesis, 745 (1–2) (2012) 84-91.
10. Noguera C., “Physics and Chemistry at Oxide Surfaces”, Cambridge, (1996) (15) 223.
11. Ayyub P., Palkar V. R., Chattopadhyay S., Multani M., “Effect of crystal size reduction on lattice symmetry and cooperative properties”, Physical Review B, 1995, 51(9) (1995) 6135-6138.
12. Franke M.E., Koplin T.J., Simon U., “Metal and metal oxide nanoparticles in chemiresistors: does the nanoscale matter?”, Small, 2(1) (2006) 36–50.
13. Rodriguez J.A., Wang., Hanson J.C., Liu G., Iglesias-Juez A., Fernandez Garcıa M., “The behavior of mixed-metal oxides: Structural and electronic properties of Ce1-xCaxO2 and Ce1-xCaxO2-x”, Journal of Chemical Physics, 119(11) (2003) 5659-5669.
14. Bansal V., Poddar P., Ahmad A., Sastry M., “Room-temperature biosynthesis of ferroelectric barium titanate nanoparticles”, Journal of the American Chemical Society, 128(36) (2006) 11958–11963.
15. Rodriguez J.A., Chaturvedi S., Kuhn M., Hrbek J., “Reaction of H2S and S2 with Metal/Oxide Surfaces: Band-Gap Size and Chemical Reactivity”, The Journal of Physical Chemistry B, 102(28) (1998) 5511-5519.
16. Rustum R., Ronnen R.A., Roy D.M., “Alternative perspectives on "quasi crystallinity": non-uniformity and nanocomposites”, Materials Letters, 4 (8-9) (1986) 323-328.
17. Pokropivnyi V.V., “Two-dimensional nanocomposites: photonic crystals and nanomembranes (review): Types and preparation”, Powder Metallurgy and Metal Ceramics, 41(5-6) (200) 264-272.
18. Allen M.J., Tung V.C., Kaner R.B., “Honeycomb carbon: A review of graphene”, Chemical Reviews, 110 (1) (2010) 132-145. 145
19. Vairavapandian D., Vichchulada P., Lay M.D., “Preparation and modification of carbon nanotubes: Review of recent advances and applications in catalysis and sensing”, Analytica Chimica Acta, 626(2) (2008) 119-129.
20. Potts J. R., Dreyer D. R., Bielawski C. W., Ruoff R. S., “Graphene-based polymer nanocomposites”, Polymer, 52(1) (2011) 5-25.
21. Geim A. K., Novoselov K. S., “The rise of graphene,” Nature Materials, 6 (3) (2007) 183-191.
22. Compton O. C., Nguyen S. T., “Graphene oxide, highly reduced graphene oxide, graphene: versatile building blocks for carbon-based materials,” Small, 6 (6) (2010) 711–723.
23. Ge S., Shi X., Sun K., Li C., Uher C., Baker J.R., Holl M.M.B., Orr B.G., “Facile Hydrothermal Synthesis of Iron Oxide Nanoparticles with Tunable Magnetic Properties”, The Journal of Physical Chemistry C, 113(31) (2009) 13593-13599.
24. Kitamura Y., Okinaka N., Shibayama T., Mahaney O.O.P., Kusano D., Ohtani B., Akiyama T., “Combustion synthesis of TiO2 nanoparticles as photocatalyst”, Powder Technology, 176(2-3) (2007) 93-98.
25. Jones A. C., Chalker P. R., “Some recent developments in the chemical vapour deposition of electroceramic oxides”, Journal of Physics D: Applied Physics, 36(6) (2003) 80-95.
26. Watson S., Beydoun D., Scott J., Amal R., “Studies on the Preparation of Magnetic Photocatalysts”, Journal of Nanoparticles Research, 7(6) (2005) 691-705.
27. Whitesides G.M., Grzybowski B., “Self-Assembly at All Scales”, Science, 295(5564) (2002) 2418-2421.
28. Kamien R. D., “Topology from the Bottom Up”, Science, 299(5613) (2003) 1671-1673. 146
29. Adlim A., “Review: Preparations and application of metal nanoparticles”, Indonesian Journal of Chemistry, 6(1) (2006) 1-10.
30. Manoj B.G., Goswami A., Felpin F.X., Asefa T., Huang X., Silva R., Zou X., Zboril R., Varma R.S., “Cu and Cu-Based Nanoparticles: Synthesis and Applications in Catalysis”, Chemical Reviews, 116(6) (2016) 3722-3811.